Journal of Nuclear Materials 540 (2020) 152380

Contents lists available at ScienceDirect

Journal of Nuclear Materials

journal homepage: www.elsevier.com/locate/jnucmat

Effects of carbon doping on irradiation resistance of $Fe_{38}Mn_{40}Ni_{11}Al_4Cr_7$ high entropy alloys

Shangkun Shen [a, c], Feida Chen [a, c], Xiaobin Tang [a, b, *], Jiwei Lin [a], Guojia Ge [a, b], Jian Liu [a]

[a] Department of Nuclear Science & Technology, Nanjing University of Aeronautics and Astronautics, Nanjing, 211106, China
[b] Key Laboratory of Nuclear Technology Application and Radiation Protection in Astronautics, Nanjing University of Aeronautics and Astronautics, Ministry of Industry and Information Technology, Nanjing, 211106, China
[c] Jiangsu Engineering Laboratory of Nuclear Energy Equipment Materials, Nanjing, 211106, China

ARTICLE INFO

Article history:
Received 5 December 2019
Received in revised form
18 May 2020
Accepted 2 July 2020
Available online 16 July 2020

Keywords:
Carbon doped HEAs
Interstitial carbon
Heavy-ion irradiation
Dislocation loop
Hardening resistance

ABSTRACT

High-entropy alloys (HEAs) have become newly emerging candidates as structural materials of advanced fission reactor because of their excellent mechanical properties and irradiation resistance. Recently, carbon doped HEAs exhibited improved mechanical properties, such as yield strength and elongation. However, the effects of carbon doping on the irradiation resistance of HEAs need further investigation. Here, the irradiation-induced defects and irradiation hardening of $Fe_{38}Mn_{40}Ni_{11}Al_4Cr_7$ HEA with different carbon contents were investigated by using 5 MeV Xe^{23+} heavy-ion irradiation at room temperature, and multiple characterization methods were used to provide the essential evidences. Results showed that the carbon doped samples exhibited smaller-sized dislocation loops and significantly lower hardening rate than those of undoped samples. The reason is attributed to two aspects: Firstly, interstitial carbon would significantly increase lattice distortion and migration energy of self-interstitial atoms, thereby inhibiting the formation of defects. Secondly, carbon atoms would act as obstacles that hindered the evolution of defects. Consequently, our study indicated the potential of using carbon doped HEAs as irradiation-resistant materials.

1. Introduction

The rapid development of advanced nuclear power technology has raised new demands and challenges for structural materials in aggressive environments [1,2]. Recently, a novel class of advanced irradiation-resistant materials, which is classified as high-entropy alloys (HEAs), have elicited widespread attention. Unlike conventional alloys, HEAs are solid solutions of simple-phase structure formed by multiple principle elements [3,4]. Based on previous studies, the solid solution of most HEAs can be divided into substitutional and interstitial solid solutions [6]. At present, most research on mechanical properties and irradiation resistance focus on substitutional solid solution HEAs, whereas studies on interstitial HEAs are very limited [5,6].

Similar to substitutional strengthening in HEAs, interstitial alloying is also used to improve the mechanical properties of HEAs [7]. Conversely, the small-sized interstitial atoms can cause large lattice distortion in HEAs. Therefore, the strengthening effect of interstitial atoms on HEAs is significantly higher than that in substitutional solid solution strengthening. For example, Wu et al. [5] dissolved carbon in FeNiCoCrMn, and the results showed that the yield strength and the ultimate tensile strength significantly increased. Stepanov et al. [8] added 0.1 at. % carbon in FeCoNiCrMn, and found that the strength of carbon doped alloys was improved, and high plasticity was retained. Wang et al. [9] reported that the yield strength of $Fe_{40.4}Ni_{11.3}Mn_{34.8}Al_{7.5}Cr_6$ HEAs doped with 1.1 at. % carbon increased from 159 MPa to 355 MPa in comparsion with undoped alloys.

The promising irradiation resistance of HEAs derived from the particularity of their crystal structures. Severe lattice distortion effect with high configurational entropy of HEAs results in the sluggish diffusion of interstitials [10–12]. For example, Kumar et al. [13] investigated the microstructural stability of FeNiMnCr HEA under ion irradiation, and found that no phase instability was observed at 400–700 °C when the irradiation dose reached 10 dpa. G. Velişa et al. [14] recently observed the suppressed damage

* Corresponding author. Department of Nuclear Science & Technology, Nanjing University of Aeronautics and Astronautics, Nanjing, 211106, China.
E-mail address: tangxiaobin@nuaa.edu.cn (X. Tang).

https://doi.org/10.1016/j.jnucmat.2020.152380
0022-3115/

accumulation of NiFeCoCr under ion irradiation at low temperature (16 K), suggesting that the self-healing is an intrinsic property rather than a thermally activated process of multiprincipal alloys. Lu et al. [15] found that the interstitial atoms exhibited a 3D motion migration mode in NiFe, and 1D motion in pure Ni. Accordingly, lattice distortion and high entropy effects can significantly reduce the migration ability of interstitial atoms and promote the recovery of irradiation-induced defects; as such, the growth of vacancy cluster is suppressed, and the size of helium cavities in HEAs is smaller under ion irradiation compared to conventional alloys [15–17]. Therefore, the increase in the lattice distortion of HEAs through the addition of interstitial carbon may further improve its irradiation resistance.

Fe–Mn–Ni–Al–Cr HEAs, which are similar to those in the report of Wang et al. [9,18], were selected in this work. Carbon doped $Fe_{38}Mn_{40}Ni_{11}Al_4Cr_7$ HEAs were irradiated at room temperature under 5 MeV Xe^{23+} ions to investigate the phase stability, defects evolution and irradiation-induced hardening of carbon doped HEAs. In addition, X-ray diffraction (XRD), grazing incidence X-ray diffraction (GIXRD), scanning electron microscopy (SEM), transmission electron microscopy (TEM), and nanoindentation were used to provide essential experimental data.

2. Materials and experiments

2.1. Alloys and ion irradiation

Four types of HEAs based on $Fe_{38}Mn_{40}Ni_{11}Al_4Cr_7$ doped with 0 at. %, 0.2 at. %, 0.5 at. % and 1.0 at. % carbon were used in our work. To produce these alloys, pieces of Fe, Mn, Ni, Al, Cr and Fe_3C (>99.9% pure) were accurately weighed and mixed via vacuum levitation melting process, which has several advantages in smelting complex alloys [19]. To ensure the accuracy and homogeneity of all the components, additional 5 wt % Mn was added, and every ingot was re-melted at least four times before being drop-casted into a copper mold. Finally, the ingots were cut into pieces with thickness of 1.0 mm and then chemically-mechanically polished to a mirror surface. In order to eliminate the internal stress caused by the preparation, all the polished samples were annealed at 530 °C for 4 h with high vacuum of 10^{-5} Pa. In the following, C0, C0.2, C0.5 and C1.0 are used to represent 0 at. %, 0.2 at. %, 0.5 at. % and 1.0 at. % carbon doped samples, respectively.

The irradiation experiments were performed on the 320 kV platform at the Institute of Modern Physics, Chinese Academy of Sciences (CAS). The four types HEAs of C0, C0.2, C0.5 and C1.0 samples were irradiated with 5 MeV Xe^{23+} ions to fluences of 3.65×10^{14}, 1.4×10^{15}, and 3.65×10^{15} ions/cm^2 (corresponding to approximately 1, 3.8 and 10 dpa, respectively) at room temperature with vacuum of 10^{-5} Pa. As shown in Fig. 1 (b), to ensure the same irradiation conditions of the samples, four samples with different carbon contents (C0, C0.2, C0.5 and C1.0) were placed under the same beam spot. The corresponding displacements per atom (dpa) as a function of depth were speculated using SRIM-2013 program at the Quick Kinchin-Pease Model with 25 eV displacement threshold energy (E_d) for aluminum element and 40 eV for other elements [20,21]. In the calculations, the target compositions were set to be consisting with Table 1, and the density of targets were assumed to be 7.35 g/cm^3. Given that the slight changes in composition have neligible effects on the calculation results of SRIM, only the calculation results of C0.5 were shown in Fig. 1 (a).

Table 1
The average chemical composition of the resulting ingots from the upper, middle and bottom measured by using OES (in at. %). In addition, the specific chemical composition at the upper, middle and bottom of each resulting ingot can be found in Table S1 of Supplementary material.

Conc. (at.%)	Fe	Mn	Ni	Al	Cr	C
C0	38.82	40.38	10.81	3.10	6.86	0.03
C0.2	37.63	41.02	11.01	3.38	6.75	0.21
C0.5	38.12	40.30	10.67	3.61	6.78	0.52
C1.0	37.77	40.54	10.42	3.56	6.66	1.05

2.2. Characterization

The chemical compositions of the resulting ingots were measured using optical emission spectrometer (OES, SPECTRO MAXx with stationary metal analyzer), and the results were shown in Table 1. To verify the homogeneity of components and ensure the accuracy of the results, each alloy was tested three times, and the test samples were taken from the upper, middle and bottom of the ingots, respectively. The phase structures of polished as-cast samples were identified by conventional XRD (Rigaku Ultima IV with Cu K-alpha radiation) operated at 40 kV voltage, 40 mA current, and 0.01 step size. In order to calculate the lattice parameter using Bragg law, the wavelength of X-ray was calibrated with standard Si, and then the positions of all the diffraction peaks were measured on the diffractogram. In addition, GIXRD (Bruker D8 ADVANCE with Cu K-alpha radiation) measurements were performed to investigate the phase stability of irradiated regions. The X-ray scanning ranges were set from 20° to 100° with 0.01 step size. The penetration depth of GIXRD was adjusted to approximately 1.2 μm by fixing the incident beam at 1° relative to the sample surface. However, considering the limitation of the detection instrument, minor phases were not detectable when its volumes ≤5 wt %.

The microstructures of the polished and etched samples were characterized via SEM (TESCAN LYRA3 GM at a working voltage of 20 kV), and Energy Dispersive X-ray Spectroscopy (EDS) was used to analyze the distribution of elements. The ferric chloride solution

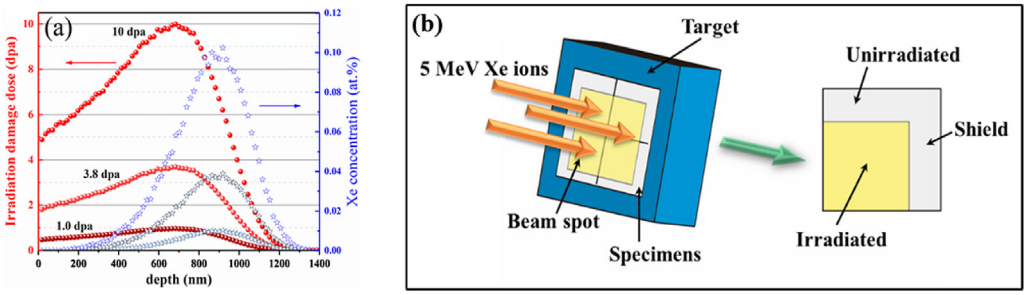

Fig. 1. (a) Calculation results of irradiation damage dose as a function of depth for C0.5 with 5 MeV Xe^{23+} to a fluence from 3.65×10^{14} cm^{-2} to 3.65×10^{15} cm^{-2}. (b) diagram of irradiation experiment.

with 10% nitric acid was used as etching solution for all the samples. In addition, Focused Ion Beam (FIB) technique was used for the preparation of TEM foils. The foils were prepared through trenching and initial thinning with 30 keV Ga ions, and then the energy of ions was reduced to 5 keV to remove the ion-induced surface amorphous layer. Subsequently, the final milling was performed with 2 keV Ga ions to reduce the damage caused by FIB process in the TEM foils. After measurement by FIB workstation, the thickness of TEM foils is about 59.4−64.8 nm. The irradiation-induced defects were evaluated by TEM (FEI Talos F200X operated at 200 kV with two-beam conditions) both in bright field (BF) and dark field (DF). Weak-beam dark field (WBDF) images with **g**/3**g** diffracting condition were used to observe the irradiation-induced dislocation loops. The size and density of dislocation loops were calculated in the Nano-measurement software. In order to ensure the accuracy of the statistical results for each sample, the size and number densities data of dislocation loops were derived from at least ten TEM images.

Nanoindentation tests (Nano Indenter G200, Agilent) for the samples before and after irradiation were performed at Suzhou Institute of Nano-Tech and Nano-Bionics, CAS. The continuous stiffness measurement (CSM) with a Berkovich-type indenter [22−24] was adopted in the tests. The maximum indentation depth and load were set to 1800 nm and 230 mN, respectively. The average nanohardness of each sample was calculated by using five indentation tests to avoid accidents.

3. Results and discussion

3.1. Microstructures

As shown in Table 1, the normalized average contents of Fe, Ni, Mn, Al, Cr and C in the alloys were basically as expected, indicating the accuracy of the smelting process. Among them, the contents of carbon in each ingot were slightly higher than expectation, because the metals, especially Fe and Mn, would inevitably bring trace amount of carbon impurities during smelting process. However, due to its low concentration, the effects of the trace carbon impurities were ignored in our work. As shown in Table S1 of supplementary material, the content of each element measured from the upper, middle and bottom of each ingot exhibited slight deviations, suggesting that the chemical compositions of the alloys were homogenous. In addition, Fig. 2 (a) shows the XRD data from pristine $Fe_{38}Mn_{40}Ni_{11}Al_4Cr_7$ HEAs with different carbon contents. The XRD patterns proved that all alloys were single phase with face-centered-cubic (FCC) structure, and the Bragg angle for diffraction peaks of each sample slightly decreased with the increase in carbon content. Correspondingly, the lattice parameter ***a***, which were determined from the XRD data, almost linearly increased with increasing carbon concentration (Fig. 2 (b)), thereby further confirmed that the carbon dissolved in the interstices of the FCC lattice [11]. The error bars in Fig. 2 (b) were due to slight deviations in the lattice parameter values calculated from the different diffraction peaks.

In particular, the HEAs in our work contain many carbide-forming elements, such as Fe, Mn, Cr, etc., but any detectable phase decomposition or precipitation was not found by XRD. This phenomenon may be attributed to the unique high entropy effect [25] and sluggish diffusion effect [26] of HEAs. Based on previous research, the above two effects would significantly inhibit the migration of solute atoms in HEAs, thereby hindering the formation of new phases. Moreover, Li [27] reported that the increase of carbon content leads to significantly higher energy barrier to recrystallization of HEAs during annealing. Therefore, under similar processing conditions, no detectable carbides were found by XRD in carbon doped HEAs as in austenitic steels.

Fig. S1 in Supplementary material shows the mircostruction of initial samples with different carbon contents. It can be found that the samples have a number of inevitable as-cast defects, such as holes, which may be related to the rapid cooling rate of the samples during solidification, however, the test areas of FIB process and nanoindentation were selected far away from these defects. Notably, the samples with different carbon contents exhibit different grain size: as the carbon content increase, the grain size of the samples gradually decrease, which is similar with the report by Gou et al. [28]. It is very difficult to accurately calculate the average grain size in the SEM images, so we estimated the lower limit of the grain size of C0, C0.2, C0.5 and C1.0 samples, which are 230 μm, 200 μm, 180 μm and 150 μm, respectively. This result is due to the fact that carbon atoms provide more heterogeneous nucleation sites and have pinning effect on the grain boundaries (GBs) [29] thereby inhibiting the growth of the grains during the solidification. Carbon doping further inhibits the migration of solute atoms, which may increase the segregation tendency of initial samples at GBs. We conducted EDS for the grain boundary of C1.0 sample to explore the element distribution at the GBs. For details, see Fig. S2 and Fig. S3 in Supplementary material. Similar phenomenon of segregation was reported in recent research [30].The discussion of composition segregation in pristine C1.0 can be found in Supplementary material.

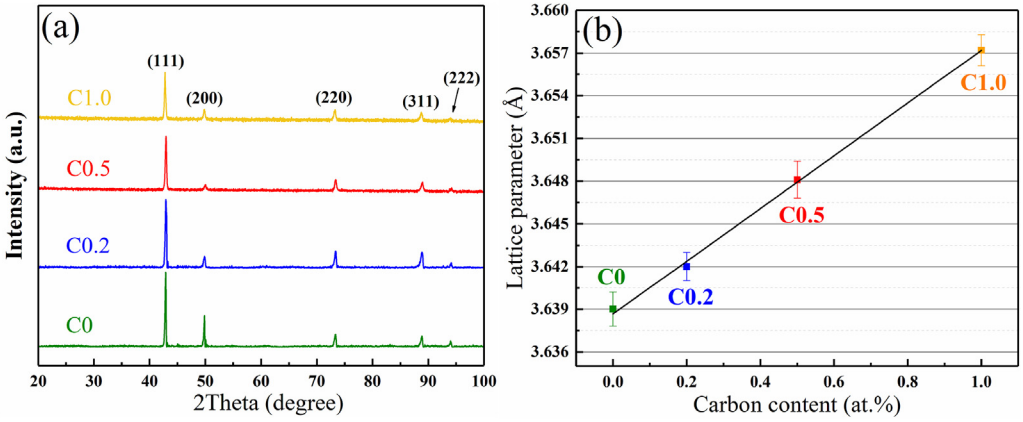

Fig. 2. (a) XRD patterns from pristine C0, C0.2, C0.5 and C1.0. (b) Lattice parameter versus carbon content determined from XRD data.

3.2. Phase stability

Unlike the trace of carbide precipitations of pristine C1.0, the irradiation-induced phase transitions are extensive and can be detected by X-ray diffraction. In accordance with the calculation results of SRIM, the maximum incident depth is approximately 1400 nm under 5 MeV Xe^{23+} ion irradiation. The potential phase transition and structural change in the irradiated damaged layer can be evaluated using GIXRD.

The GIXRD patterns of irradiated samples with different carbon contents (Fig. 3) show severa. l FCC austenite diffraction peaks of γ (111), γ (200), γ (220), γ (311) and γ (222). No other new detectable diffraction peaks appear (Fig. 3(a)), indicating that all the alloys remained single phase with FCC structure after irradiation to fluences of 1.4×10^{15} ions/cm^2. As the irradiation fluence increased to 3.65×10^{15} ions/cm^2, no visible phase transformation or decomposition of C0.5 occurred in Fig. 3 (b). These results suggested the irradiated region of the samples remained fully crystalline and retained the original FCC phase, with no detectable second phase observed as a function of irradiation dose up from 1 dpa to 10 dpa at room temperature. Similar results have been reported in several recent studies [13,31].

However, unlike austenitic steels after Xe^{+} ion irradiation [32], the diffraction peaks of C0.5 did not show a reduction in 2θ with the increase in irradiation dose; as such, the lattice parameter value of C0.5 remained unchanged after irradiation. Moreover, the intensity and FWHM of the diffraction peaks did not change significantly, indicating that the crystal structure and interstitial carbon atoms were stable under 5 MeV Xe^{23+} irradiation at room temperature. Overall, the GIXRD results proved that phase transitions were not observed at any irradiation conditions in our work. Thus, the changes in microstructure and nanohardness were mainly caused by the formation and evolution of irradiation-induced defects under irradiation rather than phase transitions or precipitation. In response to this conclusion, the following discussion would explain the specific contribution of carbon doping in irradiation resistance from two aspects.

3.3. Irradiation-induced defects

As shown in Fig. S4 of Supplementary material, almost no defects were observed in the unirradiated samples, and the effects of the original defects in the samples are negligible in our work because of their low volume fraction. In addition, we did not observe any nano-precipitates from TEM images, indicating that the influence of the interface between precipitates and matrix on the evolution of defects can be neglected. Irradiation-induced defects of materials mainly include voids, dislocation loops and chemical segregation. Among them, dislocation loop is generally the most typical defect in irradiated materials [33]. Therefore, we characterized and analyzed the irradiation-induced dislocation loop in the samples with different carbon contents, revealing the effect of interstitial carbon on the irradiation resistance of HEAs.

Fig. 4 shows the defect bands of the samples irradiated at room temperature to a fluence of 1.4×10^{15} ions/cm^2, which corresponds to the peak damage dose of 3.8 dpa. It can be seen from the images that there are obvious differences in the irradiation-induced defects of the samples with different carbon contents under the same irradiation condition. Specifically, the defect bands of the irradiated C0 and C0.2 samples are concentrated in the depth region between 580 and 750 nm, which is consistent with the SRIM calculation results, however, the irradiation-induced defects of C0.5 and C1.0 samples exhibit higher-density dispersion compared to C0 and C0.2 samples, which are mainly distributed at the depth of 500–820 nm. In addition, the irradiation-induced defects show different microstructures in samples with different carbon contents. Obviously, the defects in C0 and C0.2 samples are mainly large-sized dislocation loops and dislocation lines, while those in C0.5 and C1.0 samples are small-sized dislocation loops and black dots defects. It is worth mentioning that black dots in our work are considered to be small-sized dislocation loops or defect clusters. This result indicates that carbon doping may have a great influence on the evolution of irradiation-induced defects at room temperature. From the perspective of the defect distribution, the effect is manifested as: pinning irradiation-induced defects and inhibiting their migration or accumulation, resulting in a higher defect density and smaller defect size of the doped samples than those of undoped sample. The figures inserted in Fig. 4 (a)–(d) show the SAED patterns of C0, C0.2, C0.5 and C1.0 samples after irradiation. It can be seen that all the SAED patterns of the irradiated samples maintain single-phase with FCC, and any detectable phase decomposition or precipitation was not found, which is consistent with the results of GIXRD.

Fig. 5 shows the statistical results of dislocation loop size and number density. The dislocation loop size was determined by measuring the longest axis, and the standard derivation in this result is attributed to the uncertainties in dislocation loop identification during the statistical process. To ensure accuracy, the statistical results of each sample were from at least ten TEM images. According to the statistical results, we found that with the increase of carbon content, the size of the dislocation loops gradually decreased, while the density increased. The average sizes of dislocation loops in C0 and C0.2 samples are around 14.11 nm and

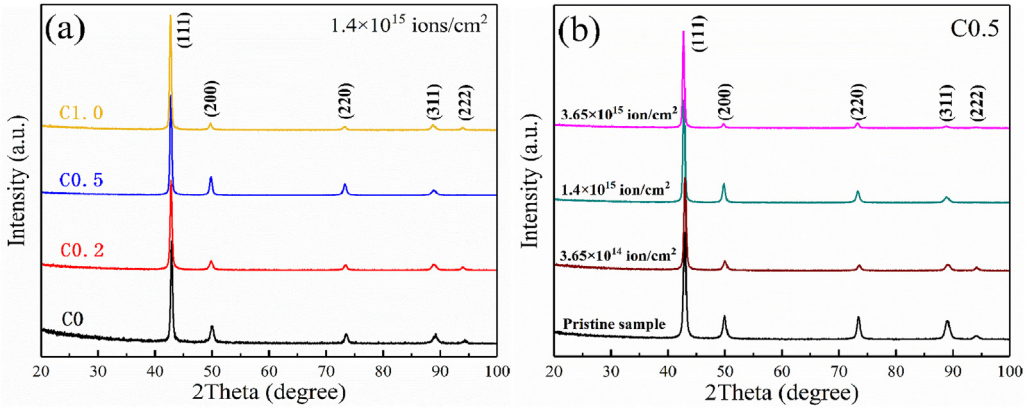

Fig. 3. GIXRD patterns for pristine and irradiated samples: (a) Samples with different carbon contents under 5 MeV Xe^{23+} irradiation to a fluence of 1.4×10^{15} cm^{-2}. All the samples maintain FCC. (b) Pristine C0.5 and C0.5 irradiated fluence from 3.65×10^{14} cm^{-2} to 3.65×10^{15} cm^{-2}.

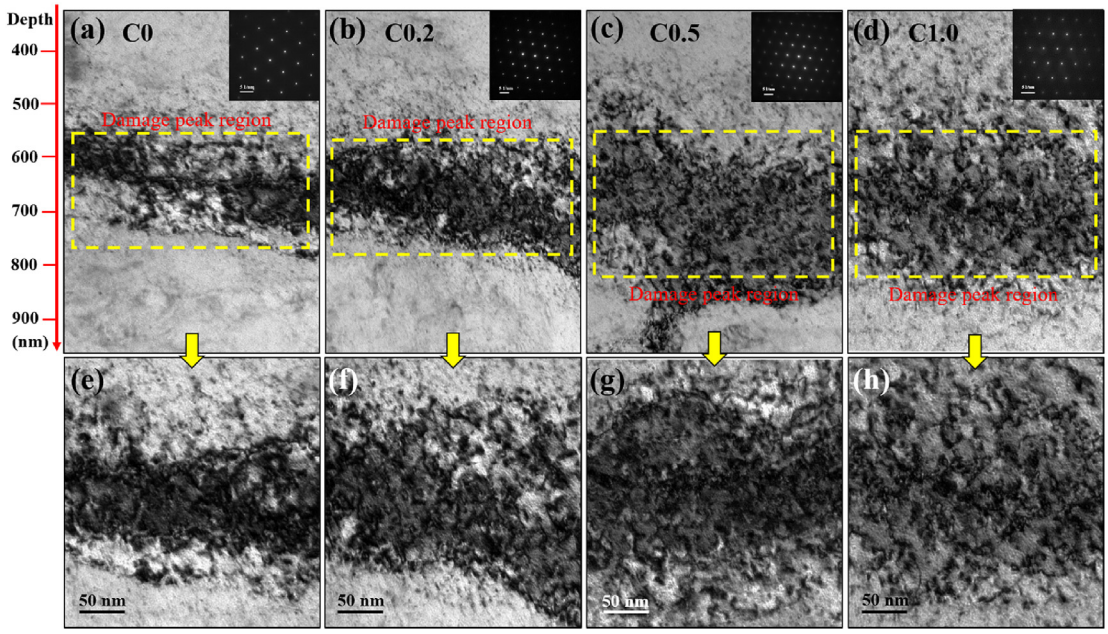

Fig. 4. Defect bands BF-TEM images at damage peak region (marked by the yellow frame) of irradiated samples at fluence to 1.4×10^{15} cm^{-2}. (a) C0, (b) C0.2, (c) C0.5, (d) C1.0. The figures inserted in (a)–(d) are selected area electrom diffraction (SAED) patterns corresponding to the sample after irradiation. (e)–(h) are the enlarged images of (a)–(d), respectively. All the images were taken near the [011] zone axis with **g** = 200. (For interpretation of the references to colour in this figure legend, the reader is referred to the Web version of this article.)

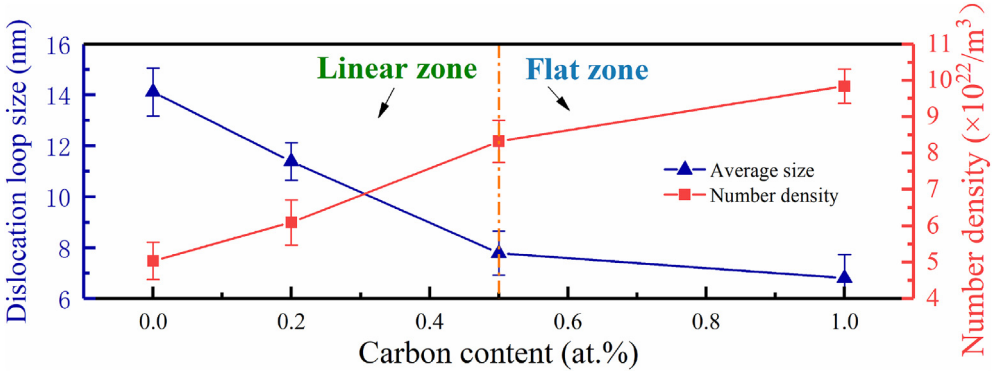

Fig. 5. Statistical results of the size and number densities of observed dislocation loops for the samples with different carbon contents irradiated at fluence to 1.4×10^{15} cm^{-2}.

11.38 nm, whereas that in C0.5 and C1.0 samples are only 7.91 nm and 6.82 nm, respectively. Furthermore, the number densities of dislocation loops in C0, C0.2, C0.5 and C1.0 samples were estimated to be 5.04×10^{22}/m^3, 6.10×10^{22}/m^3, 8.32×10^{22}/m^3 and 9.84×10^{22}/m^3, respectively. The above results of dislocation loops are similar with previous studies on FCC austenite materials [13,32,34,35]. It is worth noting that the decrease in dislocation loop size and the increase in number density are almost linear when the carbon content is lower than 0.5 at. % (linear zone in Fig. 5), but when the carbon content continues to increase, the response of irradiation defects to carbon content is weakened (flat zone in Fig. 5). This phenomenon may be due to the number density of defects, such as dislocation loops, reaching saturation under the irradiation condition in our work. Edwards et al. [36] reported that the dislocation loops of austenitic steels irradiated at a low temperature (less than 300 °C) would reach a saturation density of about 10^{23}/m^3, which is consistent with our results.

Fig. 6 (a)–(h) show the morphology of dislocation loops at the damage peak region in samples with different carbon contents. Among them, Fig. 6 (b), (d), (f) and (h) are weak-beam (g/3g) DF mircographs, and the white dots in DF images correspond to the black defects in BF images. This phenomenon indicates and verifies that the formation of irradiation-induced dislocation loops in the samples irradiated by 5 MeV Xe^{23+} to the fluence of 1.4×10^{15} cm^2 at room temperature. These dislocation loops are mainly interstitial-type dislocation loops, which caused by the accumulation of self-interstitial atoms or clusters. Specifically, 5 MeV Xe ions irradiation caused collision cascades and created interstitial atoms. These interstitial atoms accumulated into defect clusters, and the clusters continue to absorb interstitial atoms or other clusters, eventually forming dislocation loops. By comparative study, we found that the dislocation loops observed in undoped sample are clustered and form large-sized defects. But, as the carbon content increases, the number of large-size defects decreases, and the distribution of dislocation loops become dispersed. Very low density of dislocation lines or dislocation lines are observed in C0.5 and C1.0, but plenty of small-sized defects (corresponding to the white dots in weak-beam DF TEM images) are observed. This

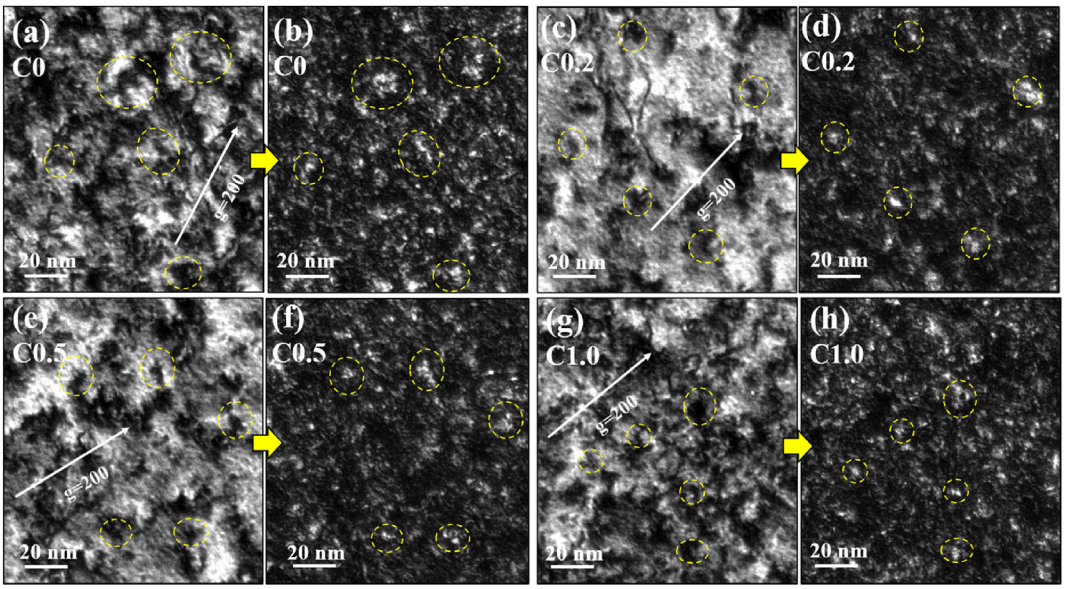

Fig. 6. Enlarged BF and weak-beam DF TEM images of all the samples irradiated by 5 MeV Xe^{23+} ions with dose of 1.4×10^{15} cm^2. (a), (c), (e) and (g) are BF images of C0, C0.2, C0.5 and C1.0 samples, respectively. (b), (d), (f) and (h) are the corresponding weak-beam DF (**g**/3**g**) images. All the images were taken near the [011] zone axis with **g** = 200. Some dislocation loops were highlighted respectively by yellow circles. (For interpretation of the references to colour in this figure legend, the reader is referred to the Web version of this article.)

phenomenon shows that the interstitial carbon dose not affect the good irradiation resistance of HEAs, but has the effect of suppressing the clustering process of defects instead, which may further improve the irradiation resistance of HEAs. By analyzing the formation process of dislocation loops, the above results of HEAs doped with different carbon contents can be explained in the nucleation and growth stage of dislocation loops. In the nucleation stage, interstitial carbon atoms could capture the defect clusters and provide more nucleation sites. Lu et al. [37] recently reported that interstitial carbon promotes the recombination of interstitial atoms and vacancy defect pairs and suppresses the irradiation-induced primary damage formation, thereby reducing the number of self-interstitial atoms that can be absorbed by defect clusters. Compared to undoped sample, this may result in smaller dislocation loop size and greater number density of carbon doped samples. The growth of dislocation loops is the accumulation of point defects or defect clusters, which is mainly dominated by the migration ability of the defects. In FCC structure materials, the migration of the point defect can be commonly explained as the vacancy and interstitial mechanisms, and the atomic self-diffusion coefficient of the mechanism can be expressed as Eq. (1).

$$D_\theta^a = \alpha a^2 \nu exp\left(\frac{S_\theta^f + S_\theta^m}{k}\right)\exp\left(\frac{-E_\theta^f - E_\theta^m}{kT}\right) \quad (1)$$

where $\boldsymbol{\alpha} = zA^2/6$; $\nu = 10^{13}/s$; $\boldsymbol{a}$ is the lattice parameter; $\boldsymbol{z}$ is the coordination number; $\boldsymbol{\theta} = \boldsymbol{v}$ and $\boldsymbol{i}$ represents the vacancy and interstitial atoms, respectively; S^m and E^m are the migration entropy and migration energy of the point defect, respectively; and S^f and E^f are the formation entropy and formation energy of the point defect, respectively. Eq. (1) shows that the vacancy self-diffusion coefficient strongly depends on the migration energy. Solute atoms, such as carbon, increase the migration energy (E^m) of point defects, reduce its mobility, and affect the evolution of various defects [38]. S. Takaki et al. [39] found that the migration energy of vacancies has a low value in pure iron (0.55eV), while high values of the vacancy migration energy ($\geq$1 eV) was observed in iron containing a trace amount of carbon [40]. As such, the interaction of interstitial carbon atoms with point defects plays an important role in the microstructure evolution caused by irradiation. Terentyev D. et al. [41] examined the effects of interstitial carbon on the dislocation loops of iron under electron irradiation. The results showed that the Burgers vector of most dislocation loops was (1/2) <111>, and the dislocation loops were pinned by interstitial carbon under 250 K low-temperature irradiation. In addition, the growth of dislocation loops in FCC structure alloys was mainly through interstitial atom absorption on the <111> planes [28], which was pinned by octahedral interstitial carbon atoms. Overall, interstitial carbon atoms suppress the clustering process of irradiation-induced defects, thus reducing the size of the defects and increasing the number density.

Carbon doping improves the yield strength of alloys, but it is also likely to reduce the plasticity and corrosion resistance. Under comprehensive consideration, we believe that HEAs containing about 0.5 at. % carbon is the most valuable for research in our work. Therefore, we studied the microstructure and evolution of defects in C0.5 sample at an irradiation dose of 10 dpa. Fig. 7 (a)–(c) show the irradiation-induced defects in C0.5 sample irradiated to a fluence of 3.65×10^{15} cm^{-2}, which corresponds to the peak damage dose of 10 dpa. The high-density defects are observed in damage peak region (marked by the yellow frame), including high density of 1/3<111> faulted dislocation loops, a small number of network dislocations and dislocation tangle. According to preliminary statistics, the average size of the dislocation loops in this region is approximately 12.08 nm, which is an increase of 52.72% compared to that in C0.5 sample irradiated to the dose of 3.8 dpa. The number density of dislocation loops is estimated as $9.88 \times 10^{22}/m^3$, which is not much different from that of C0.5 sample irradiated to 3.8 dpa, only increased by 18.7%. This can be attributed to the saturation of dislocation loops under the irradiation conditions in our work. Nevertheless, the average size of dislocation loops is smaller than those in the C0 sample at an irradiation dose of 3.8 dpa, which further indicates that the interstitial carbon atoms still suppress the accumulation of irradiation defects at a high irradiation dose. This result in our work also can be corroborated by the report of Lu et al. [37]. However, in this case, the irradiation-induced defects

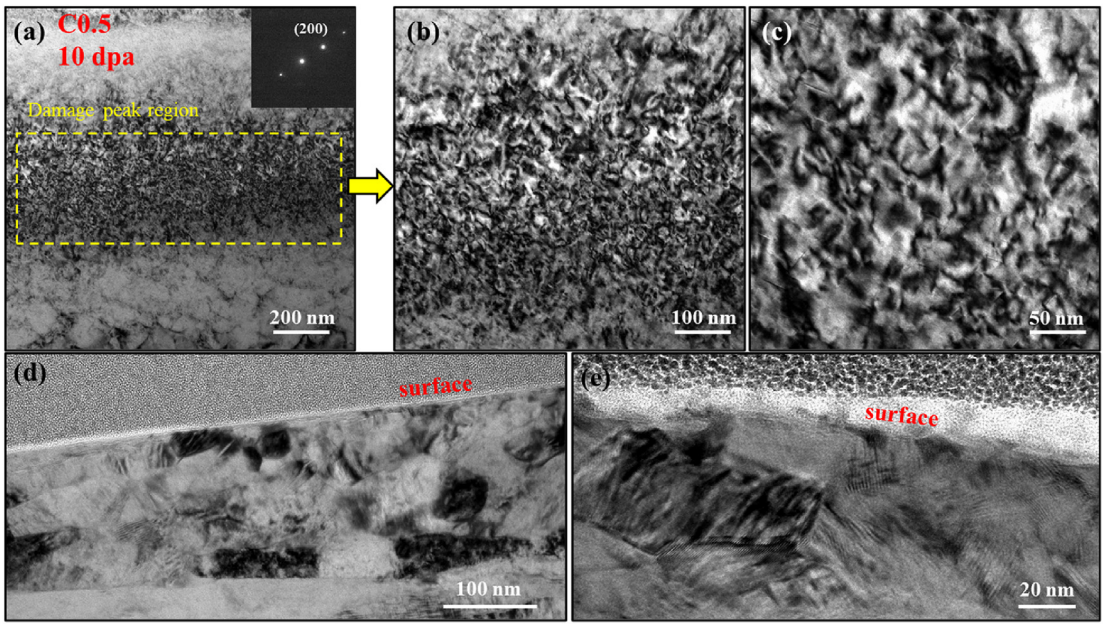

Fig. 7. TEM images for the C0.5 sample irradiated to a fluence of 3.65 × 10^{15} cm^{-2}. (a) Cross-section TEM image. (b) and (c) are micrographs at damage peak region. (d) and (e) are the surface micrographs of irradiated C0.5 sample. All the micrographs were taken near the [011] zone axis with **g** = 200.

clustered and formed a clearly visible defect band, which is quite different from the low-dose case of C0.5 sample. This may be attributed to the high irradiation dose produced an extremely large number of point defects, while the interstitial carbon content is only 0.5 at. %, which cannot provide enough nucleation sites of dislocation loops, resulting in the formation of large-sized dislocation loops caused by clustering of self-interstitial atoms. However, the specific mechanistic cannot be given in our current work, and more experiments and simulations work are needed to determine. In addition, as shown in Fig. 7 (d) and (e), the recrystallized layer of about 100–120 nm in thickness formed on the surface of C0.5 sample irradiated to 10 dpa, and some plate-like nano-precipitates can be observed in the recrystallization layer. This phenomenon is possibly due to the high irradiation dose rate (4.75 × 10^{-4} dpa/s) and the low thermal conductivity of HEAs, which caused surface temperature to be higher than expected. However, the following nanoindentation experiment removed unreliable data including this region, so the recrystallized layer would not affect any results of our work.

3.4. Nanohardness

Irradiation hardening and embrittlement occur extensively on metallic materials under irradiation. Lots of micro- and nanoscale defects could form in materials after irradiation, thereby serving as obstacles to dislocation motion and resulting in the hardening of the materials [42,43]. The depth (h) profiles of nanohardness (H) before and after alloy irradiation were characterized using nanoindentation with CSM. Fig. 8 (a)–(c) show the average nanohardness versus depth of samples with different carbon contents before and after irradiation. The nanohardness within the depth of 100 nm significantly increased and then gradually decreased until the depth reached approximately 1800 nm; these phenomena are known as the reverse indentation size effect (RISE) and indentation size effect [44], respectively [45]. Owing to the surface uncertainty of the samples and the effect of RISE, the nanohardness data corresponding to a depth of less than 120 nm should be omitted. Furthermore, in order to obtain the hardness of materials at a certain dpa, Kasada et al. proposed a method based on the Nix-Gao model for extracting the real hardness data of damaged areas by fitting curves [46,47]. Nanohardness (H_0) can be obtained from Eq. (2).

$$H = H_0\sqrt{1+\frac{h^*}{h}} \tag{2}$$

where H_0 is the hardness at infinite depth; h is the indentation depth of the indenter, and h^* is a characteristic length that depends on the shape of the indenter tip and the type of material.

The nanohardness data were plotted as the square of the hardness (H^2) and the reciprocal of the indentation depth ($1/h$) [48,49] in Fig. 8 to avoid the impact of the ISE and obtain the real hardness of the damage layer. In the case of the pristine samples and low-dose irradiated (1 dpa) samples, it can be seen that H^2 versus $1/h$ in the fitted curves showed a good linearity when the indentation depth is greater than 120 nm, indicating the hardness value of the pristine and low-dose irradiated samples did not change within the test depth range. This result was attributed to the good uniformity of hardness in pristine samples and negligible formation of irradiation-induced defects in low-dose samples. However, for the high-dose irradiated samples (3.8 and 10 dpa), the fitted curves showed evident inflection points (h_c) at approximately 300 nm, and all the curves were bi-linear. As reported in recent studies, the bi-linearity of the fitted curves is resulted from the soft substrate effect (SSE) [32,43]. Taking into account that the hemispheric influence zone of indenter can reach 4–10 times the indentation depth, that is, SSE in unirradiated region can contribute to the hardness from increasing the indentation depth [50]. As such, the inflection point of the bilinear curve represents the depth at which the SSE occurs. In the case of our work, the inflection point (300 nm) is around 1/5 of the irradiation damage layer depth (1400 nm). This can be concluded that, for the $Fe_{38}Mn_{40}Ni_{11}Al_4Cr_7$ HEA in our work, the Berkovich diamond indenter could reflect the hardness in the region of indent as well as extend down approximately five times of the contact depth.

Based on the report of Hou et al. [51], the nanoindentation

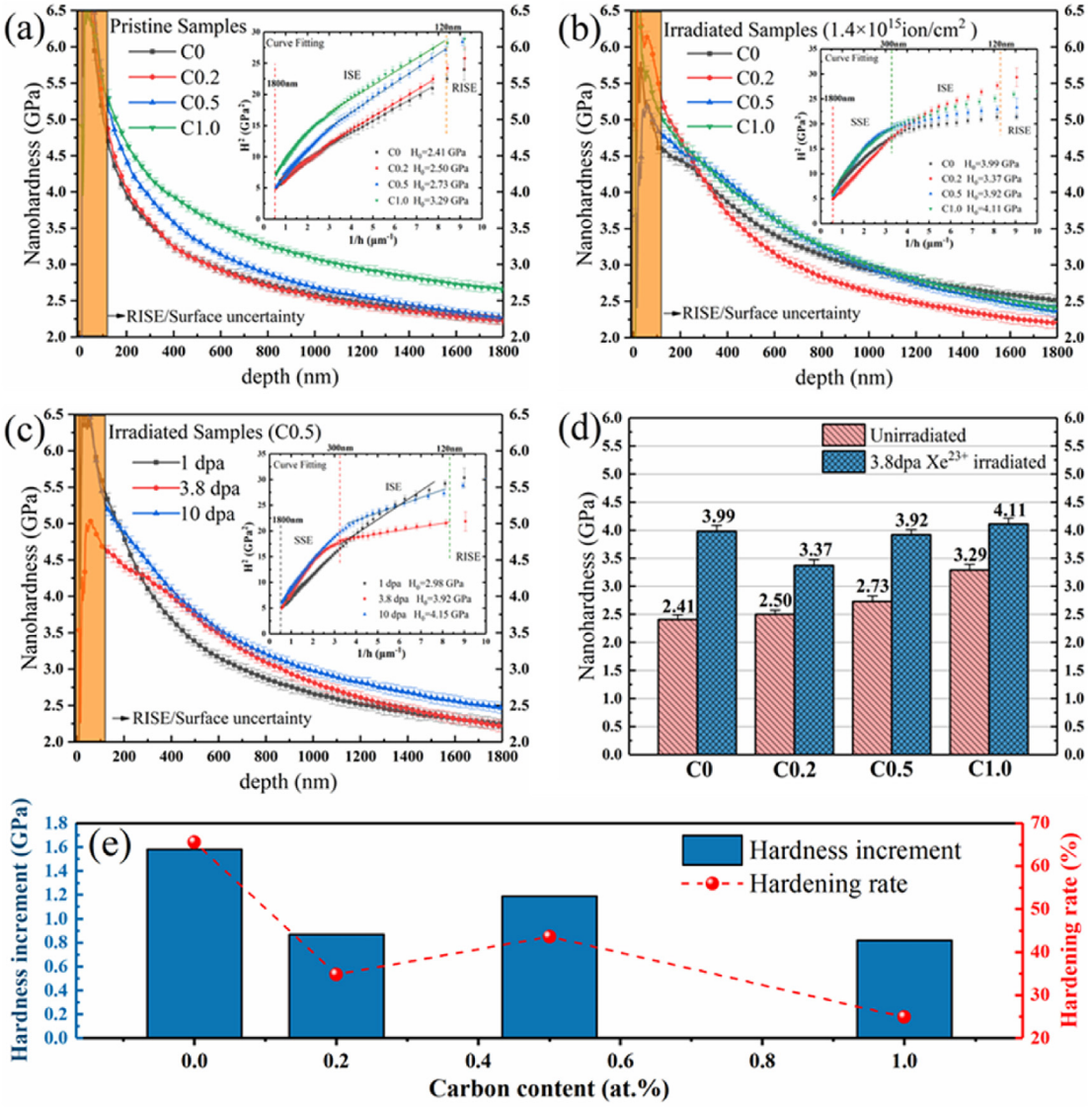

Fig. 8. Average nanoindentation hardness versus the indentation depth of C0, C0.2, C0.5, and C1.0 (a) before irradiation, (b) after irradiation fluence to 1.4×10^{15} cm^{-2} (3.8 dpa). (c) the average nanoindentation hardness versus the indentation depth of C0.5 at room temperature under the irradiation dose from 3.65×10^{14} cm^{-2} (1 dpa) to 3.65×10^{15} cm^{-2} (10 dpa). (d) Comparison of nanohardness of all the samples before and after irradiation fluence to 1.4×10^{15} cm^{-2} (3.8 dpa). (e) Hardness increment and degree of hardening of the four HEAs with different carbon contents. The figures inserted in (a)–(c) are the curves of H^2–1/h for the average nanoindentation hardness of all the samples before and after 5 MeV Xe^{23+} irradiation.

results wound not be affected by GBs when the indent size was smaller than *1/6* of the grain size. Thus, the hardness values in our work were not affected by the difference in grain size (>200 μm). Removing the data that are significantly different from the other results of each sample, the hardness of pristine samples with different carbon content (C0, C0.2, C0.5, and C1.0) were calculated as 2.41 GPa, 2.50 GPa, 2.73 GPa and 3.29 GPa, respectively. The results showed that the hardness of the samples increased with increasing carbon content. This phenomenon can be explained by two aspect: on the one side, a small amount of carbon plays a role of solid solution strengthening in alloys, which could increase the hardness. On the other side, carbon atoms could form precipitation of carbides with metal elements in alloys, and the volume fraction of carbides increases with increasing carbon content. Normally, precipitations of carbides are accompanied by hardness enhancement of alloys [52]. This finding is consistent with several previous reports [52,53]. In addition, the hardness of irradiated samples with different carbon content evidently increased with increasing dose. The irradiated region hardness of C0 increased to 3.99 GPa at 3.8 dpa, which was ~65.6% higher than that of the pristine C0. The similar results of FeNiMnCr HEA and 316 austenitic stainless steel were previously reported in Ref. [13,23,54]. However, the hardness increase rate of C1.0 after irradiation was approximately 25%, which was significantly lower than that of the C0. Similarly, more slight increase rate in hardness than that of C0 was observed in C0.2 and C0.5 samples. It is worth noting that, for all the samples, the increase of the hardness value also follows the rule described above. As such, the results of nanoindentation tests indicated that carbon doping can effectively reduce the hardness increase rate of Fe–Mn–Ni–Al–Cr HEAs after irradiation at room temperature. Specific hardness data, including unirradiated hardness (H_{un}), post-irradiation hardness (H_{irr}), increase in hardness (ΔH), and hardening rate ($\Delta H/H_{un}$) were shown in Fig. 8 (e) and Table 2.

Based on previous research, abundant irradiation-induced

Table 2
Nanohardness of samples with different carbon content before (H_{un}) and after (H_{irr}) irradiation, hardness increment after irradiation (ΔH), and the degree of hardening ($\Delta H/H_{un}$).

Sample	H_{un} (GPa)	H_{irr} (GPa)	ΔH (GPa)	$\Delta H/H_{un}$ (%)
C0	2.41	3.99	1.58	65.56
C0.2	2.50	3.37	0.87	34.80
C0.5	2.73	3.92	1.19	43.60
C1.0	3.29	4.11	0.82	24.92

defects are the main reason for the hardening of metal materials after irradiation [32]. In accordance with the mechanism of irradiation hardening, the introduction and evolution of irradiation defects, such as dislocation loops, are the root cause of hardening. The contribution of irradiation-induced defects on hardening can be interpreted by the dispersed barrier-hardening (DBH) model (Eq. (3)) [55].

$$\Delta\sigma_y = M\alpha\mu b\sqrt{Nd} \tag{3}$$

where $\Delta\sigma_y$ is the increase in yield strength; M is the Taylor factor (3.06 for equiaxed BCC and FCC structure metals); α is the defect barrier strength (~0.4 for strong obstacles); μ is the shear modulus; $\boldsymbol{b}$ is the Burgers vector of gliding dislocations; N and d are the number densities and diameter of defect cluster, respectively. In particular, the defect cluster can be considered as irradiation-induced dislocation loops in our work.

$$\Delta H = K\Delta\sigma_y \tag{4}$$

In addition, a linear relationship (Eq. (4)) of the yield strength and hardness was proven in similar FCC structure metals, such as 316 SS, and 347 SS stainless steel and FeNiMnCr HEA [13,56,57]. Based on the previous studies, the linear coefficient (K) of the FCC austenitic alloys is around 3 and remain unchanged after irradiation [57]. Simultaneous Eq. (3) and Eq. (4), there should be a positive correlation between the increase in hardness after irradiation and the product of the size and number densities value (Nd) of the irradiation defects. This can explain the different increase in hardness of the samples with different carbon contents under the same irradiation conditions: the Nd values of C0, C0.2, C0.5 and C1.0 samples were calculated to be 7.62×10^{23}, 6.94×10^{24}, 6.48×10^{23} and 6.70×10^{23}, respectively. Among them, the calculated value of C0 is much larger than that of C0.2, C0.5 and C1.0 samples. As such, it can be speculated that the irradiation-induced hardening (ΔH) of C0 sample is larger than those of C0.2, C0.5 and C1.0 samples. Given that the effects of carbon atoms in multi-component HEAs are considered extremely complicated, and it is difficult to describe the physical mechanism of interstitial carbon during irradiation by theoretical simulation or experimental observation. Regarding the specific mechanism during irradiation, it can be clearly concluded that, all the carbon doped samples showed lower increase of hardness and hardening rate than those of the undoped samples at the same irradiation conditions in our work.

In addition, the shear bands were observed in the indentations of pristine samples and low-dose irradiated C0.5. As Fig. 9 (a)–(d) show, the shear bands of C0.5 samples occurred in the pristine and 1 dpa irradiated samples, but when the damage dose reached 3.8 dpa, almost no shear bands were observed in the indentations. Fig. 9 (e) and (f) show that the shear bands were visible in the pristine C0 sample but disappeared after 3.8 dpa irradiation. In addition, irregular cracks appeared in the indentation of C0.5 after 10 dpa irradiation (shown in Fig. 9 (d)), indicating that the hardness of C0.5 increased and the plasticity significantly decreased after high-dose irradiation. Shear bands appear in the stage of good plastic deformation, and the disappearance of shear bands may indicate that the brittle transition of materials after irradiation [58,59]. As such, we can evaluate the plasticity of samples by observing the shear bands in the indentation: the denser the shear band, the better the plasticity. Overall, the disappearance of the shear bands indicated that the hardness of samples increased after irradiation, which further confirmed the results of nanohardness in our work. Fig. 9 (g) and (h) show the relationship between the hardness (and hardening rate) of C0.5 and the irradiation peak damage level, suggesting that the hardness increases with dpa value. The increases in hardness were divided into three stage (S1, S2 and S3) according to the three irradiation conditions in our work. For the S1 and S2, the hardness increase (ΔH) per change in dpa ($\Delta H/dpa$) was calculated as around 0.250 GPa/dpa and 0.314 GPa/dpa, respectively, while the $\Delta H/dpa$ decreased to 0.023 GPa/dpa at S3. Compared to traditional austenitic alloys, such as 304 SS and 316 SS [60], the $\Delta H/dpa$ values of all the stages in C0.5 are inhibited under similar irradiation conditions. Moreover, it is clear that the hardness increased quickly at the low-dose irradiation but flattened out at high-dose irradiation. This result may be attributed to the saturation of irradiation-induced defects at a certain irradiation dose. Similar experimental results were reported in previous research [42,49,60–62].

4. Conclusion

In summary, a series of experimental studies were conducted on irradiation-induced dislocation loops and hardening behavior in a group of $Fe_{38}Mn_{40}Ni_{11}Al_4Cr_7$ HEAs with different carbon contents. On this basis, we found that carbon doped HEAs exhibited improved irradiation resistance in suppression of defects evolution and resistance of hardening compared with undoped HEAs. The main conclusions of this study are presented as follows:

1. The GIXRD results showed that all the samples remained in the single phase with FCC structure after irradiation to fluences of 1.4×10^{15} ions/cm^2. No visible phase transformation or decomposition of C0.5 samples was observed with the increase in irradiation fluence to 10 dpa. The results indicated that the carbon doped $Fe_{38}Mn_{40}Ni_{11}Al_4Cr_7$ HEAs have good phase stability under irradiation, and at the same time, it proved that the changes in microstructure and nanohardness were mainly caused by the evolution of irradiation defects under irradiation rather than phase transitions and precipitation.
2. In comparison with C0, carbon doped samples exhibited smaller-sized dislocation loops and increased loop densities. Specifically, under the same irradiation conditions, as the carbon content increases, the size of the dislocation loop in damage peak region decrease and the density increase. This finding confirmed the suppression effect of carbon atoms on the formation and evolution of irradiation-induced defects. In addition, the suppression effect of interstitial carbon in growth of defects is still effective under high irradiation dose (10 dpa). However, the specific effects of interstitial carbon atoms on the irradiation defect migration energy in HEAs need further study and calculation by molecular dynamics simulation.
3. In contrast with undoped samples, carbon doped samples exhibited significantly lower increase in hardness after irradiation. The hardening rate of the C0 sample is 65.56%, whereas those of the C0.2, C0.5 and C1.0 samples are 34.8%, 43.6% and 24.92%, respectively, after irradiation dose of 3.8 dpa at room temperature. These results show that interstitial carbon can inhibit the irradiation hardening of HEAs. Moreover, the hardness increase (ΔH) per change in dpa ($\Delta H/dpa$) of C0.5 is inhibited under 5 MeV Xe^{23+} irradiation at room temperature

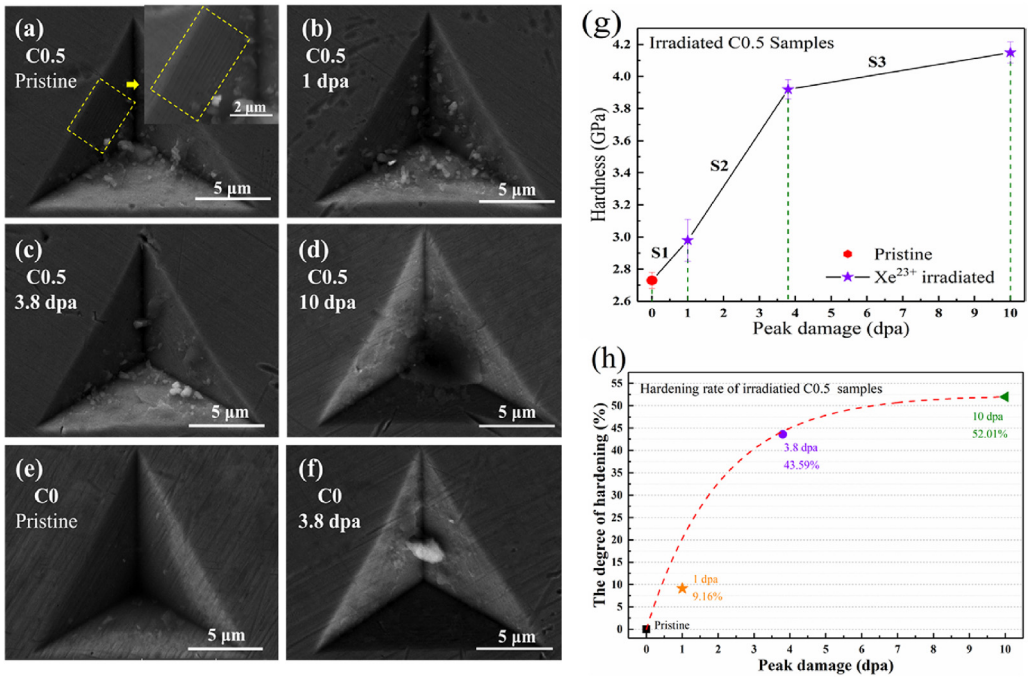

Fig. 9. Nanoindentation images of the (a) pristine C0.5 and C0.5 samples after (b) 1 dpa, (c) 3.8 dpa, (d) 10 dpa irradiation; (e) pristine C0 and (f) C0 after 3.8 dpa irradiation. (h). The hardening rate of C0.5 samples. The figures inserted in (a) depict the shear bands in the indentation of pristine C0.5; (g) Nanohardness of C0.5 samples as a function of peak damage level (dpa).

compared to other conventional alloys with similar structure and chemical composition.

Author statement

Shangkun Shen: Conceptualization, Methodology, Formal analysis, Writing-Original draft preparation, Writing-Reviewing and Editing. **Feida Chen:** Writing-Reviewing and Editing, Funding acquisition. **Xiaobin Tang:** Resources, Supervision. **Jiwei Lin:** Validation, Data Curation. **Guojia Ge:** Investigation, Data Curation. **Jian Liu:** Formal analysis, Visualization.

Declaration of competing interest

The authors declare that they have no known competing financial interests or personal relationships that could have appeared to influence the work reported in this paper.

Acknowledgments

The authors would like to thank the Institute of Modern Physics (CAS) for providing irradiation experiment. Special thanks to Senior engineer Niu of Suzhou Institute of Nano-Tech and Nano-Bionics (CAS) for his help in TEM characterization. We are grateful to Professor Min Yang of Shandong University for her help in materials preparation. In addition, this work is supported from the National Natural Science Foundation of China (Grant No. 11705087), the Natural Science Foundation of Jiangsu Province (Grant No. BK20170776), and the project supported by the Foundation of Graduate Innovation Center in NUAA (Grant No. kfjj20190604).

Appendix A. Supplementary data

Supplementary data to this article can be found online at https://doi.org/10.1016/j.jnucmat.2020.152380.

References

[1] Y. Guerin, G.S. Was, S.J. Zinkle, Materials challenges for advanced nuclear energy systems, MRS Bull. 34 (1) (2009) 10–14.
[2] H. Huang, X.B. Tang, F.D. Chen, Y.H. Yang, J. Liu, H. Li, D. Chen, Radiation damage resistance and interface stability of copper-graphene nanolayered composite, J. Nucl. Mater. 460 (2015) 16–22.
[3] J.W. Yeh, S.K. Chen, S.J. Lin, J.Y. Gan, T.S. Chin, T.T. Shun, C.H. Tsau, S.Y. Chang, Nanostructured high-entropy alloys with multiple principal elements: novel alloy design concepts and outcomes, Adv. Eng. Mater. 6 (5) (2004) 299–303.
[4] L.J. Santodonato, Y. Zhang, M. Feygenson, C.M. Parish, M.C. Gao, R.J.K. Weber, J.C. Neuefeind, Z. Tang, P.K. Liaw, Deviation from high-entropy configurations in the atomic distributions of a multi-principal-element alloy, Nat. Commun. 6 (2015) 5964.
[5] Z. Wu, C.M. Parish, H. Bei, Nano-twin mediated plasticity in carbon-containing FeNiCoCrMn high entropy alloys, J. Alloys Compd. 647 (2015) 815–822.
[6] N.D. Stepanov, D.G. Shaysultanov, G.A. Salishchev, M.A. Tikhonovsky, E.E. Oleynik, A.S. Tortika, O.N. Senkov, Effect of V content on microstructure and mechanical properties of the CoCrFeMnNiVx high entropy alloys, J. Alloys Compd. 628 (2015) 170–185.
[7] Z.M. Li, Interstitial equiatomic CoCrFeMnNi high-entropy alloys: carbon content, microstructure, and compositional homogeneity effects on deformation behavior, Acta Mater. 164 (2019) 400–412.
[8] N.D. Stepanov, D.G. Shaysultanov, R.S. Chernichenko, N.Y. Yurchenko, S.V. Zherebtsov, M.A. Tikhonovsky, G.A. Salishchev, Effect of thermomechanical processing on microstructure and mechanical properties of the carbon-containing CoCrFeNiMn high entropy alloy, J. Alloys Compd. 693 (2017) 394–405.
[9] Z. Wang, I. Baker, Z. Cai, S. Chen, J.D. Poplawsky, W. Guo, The effect of interstitial carbon on the mechanical properties and dislocation substructure evolution in Fe40.4Ni11.3Mn34.8Al7.5Cr6 high entropy alloys, Acta Mater. 120 (2016) 228–239.
[10] S. Zhao, Y. Osetsky, Y.J.A.M. Zhang, Preferential Diffusion in Concentrated Solid Solution Alloys: NiFe, NiCo and NiCoCr, vol. 128, 2017, pp. 391–399.
[11] S.J. Zhao, G. Velisa, H.Z. Xue, H.B. Bei, W.J. Weber, Y.W. Zhang, Suppression of vacancy cluster growth in concentrated solid solution alloys, Acta Mater. 125 (2017) 231–237.
[12] K.-Y. Tsai, M.-H. Tsai, J.-W.J.A.M. Yeh, Sluggish diffusion in Co–Cr–Fe–Mn–Ni high-entropy alloys 61 (13) (2013) 4887–4897.
[13] N.A.P.K. Kumar, C. Li, K.J. Leonard, H. Bei, S.J. Zinkle, Microstructural stability and mechanical behavior of FeNiMnCr high entropy alloy under ion irradiation, Acta Mater. 113 (2016) 230–244.
[14] G. Velisa, E. Wendler, S. Zhao, K. Jin, H. Bei, W.J. Weber, Y. Zhang, Delayed damage accumulation by athermal suppression of defect production in concentrated solid solution alloys, Mater Res Lett 6 (2) (2018) 136–141.
[15] C.Y. Lu, K. Jin, L.K. Beland, F.F. Zhang, T.N. Yang, L. Qiao, Y.W. Zhang, H.B. Bei,

H.M. Christen, R.E. Stoller, L.M. Wang, Direct observation of defect range and evolution in ion-irradiated single crystalline Ni and Ni binary alloys, Sci Rep-Uk 6 (2016) 19994.
[16] Z. Fan, S.J. Zhao, K. Jin, D. Chen, Y.N. Osetskiy, Y.Q. Wang, H.B. Bei, K.L. More, Y.W. Zhang, Helium irradiated cavity formation and defect energetics in Ni-based binary single-phase concentrated solid solution alloys, Acta Mater. 164 (2019) 283–292.
[17] C.Y. Lu, L.L. Niu, N.J. Chen, K. Jin, T.N. Yang, P.Y. Xiu, Y.W. Zhang, F. Gao, H.B. Bei, S. Shi, M.R. He, I.M. Robertson, W.J. Weber, L.M. Wang, Enhancing radiation tolerance by controlling defect mobility and migration pathways in multicomponent single-phase alloys, Nat. Commun. 7 (2016) 13564.
[18] Z. Wang, I. Baker, Interstitial strengthening of a f.c.c. FeNiMnAlCr high entropy alloy, Mater. Lett. 180 (2016) 153–156.
[19] B. Li, S. Zhang, J.P. Xu, W. Zhang, Development of vacuum levitation melting technology in China, Advanced Materials Research, Trans Tech Publ (2015) 406–411.
[20] R.J.M. Konings, et al., Comprehensive Nuclear Materials, Elsevier Science, 2012.
[21] R.E. Stoller, M.B. Toloczko, G.S. Was, A.G. Certain, S. Dwaraknath, F.A. Garner, On the use of SRIM for computing radiation damage exposure, Nucl. Instrum. Methods B 310 (2013) 75–80.
[22] W.C. Oliver, G.M. Pharr, An improved technique for determining hardness and elastic modulus using load and displacement sensing indentation experiments, J. Mater. Res. 7 (6) (1992) 1564–1583.
[23] X.Y. Sun, F.D. Chen, H. Huang, J.W. Lin, X.B. Tang, Effects of interfaces on the helium bubble formation and radiation hardening of an austenitic stainless steel achieved by additive manufacturing, Appl. Surf. Sci. 467 (2019) 1134–1139.
[24] F.D. Chen, X.B. Tang, H. Huang, J. Liu, H. Li, Y.L. Qiu, D. Chen, Surface damage and mechanical properties degradation of Cr/W multilayer films irradiated by Xe20+, Appl. Surf. Sci. 357 (2015) 1225–1230.
[25] D.B. Miracle, O.N. Senkov, A critical review of high entropy alloys and related concepts, Acta Mater. 122 (2017) 448–511.
[26] K.Y. Tsai, M.H. Tsai, J.W. Yeh, Sluggish diffusion in Co–Cr–Fe–Mn–Ni high-entropy alloys, Acta Mater. 61 (13) (2013) 4887–4897.
[27] Z. Li, Interstitial equiatomic CoCrFeMnNi high-entropy alloys: carbon content, microstructure, and compositional homogeneity effects on deformation behavior, Acta Mater. 164 (2019) 400–412.
[28] L. Guo, X. Ou, S. Ni, Y. Liu, M. Song, Effects of carbon on the microstructures and mechanical properties of FeCoCrNiMn high entropy alloys, Mater. Sci. Eng., A 746 (2019) 356–362.
[29] J.Y. Ko, S.I. Hong, Microstructural evolution and mechanical performance of carbon-containing CoCrFeMnNi-C high entropy alloys, J. Alloys Compd. 743 (2018) 115–125.
[30] Y.F. Ye, Q. Wang, Y.L. Zhao, Q.F. He, J. Lu, Y. Yang, Elemental segregation in solid-solution high-entropy alloys: experiments and modeling, J. Alloys Compd. 681 (2016) 167–174.
[31] M.R. He, S. Wang, S. Shi, K. Jin, H.B. Bei, K. Yasuda, S. Matsumura, K. Higashida, I.M. Robertson, Mechanisms of radiation-induced segregation in CrFeCoNi-based single-phase concentrated solid solution alloys, Acta Mater. 126 (2017) 182–193.
[32] H.F. Huang, J.J. Li, D.H. Li, R.D. Liu, G.H. Lei, Q. Huang, L. Yan, TEM, XRD and nanoindentation characterization of Xenon ion irradiation damage in austenitic stainless steels, J. Nucl. Mater. 454 (1–3) (2014) 168–172.
[33] S.J. Zinkle, L.L. Snead, Designing radiation resistance in materials for fusion energy, Annu. Rev. Mater. Res. 44 44 (2014) 241–267.
[34] S.J. Zhang, D.H. Li, H.C. Chen, G.H. Lei, H.F. Huang, W. Zhang, C.B. Wang, L. Yan, D.J. Fu, M. Tang, Ion irradiation-induced swelling and hardening effect of Hastelloy N alloy, J. Nucl. Mater. 489 (2017) 180–186.
[35] K. Shiraishi, K. Fukai, E. Yagi, Damage profiles in a stainless-steel irradiated with Ar and N ions, J. Nucl. Mater. 179 (1991) 550–553.
[36] D.J. Edwards, E.P. Simonen, S.M. Bruemmer, Evolution of fine-scale defects in stainless steels neutron-irradiated at 275 °C, J. Nucl. Mater. 317 (1) (2003) 13–31.
[37] E. Lu, I. Makkonen, K. Mizohata, Z. Li, J. Räisänen, F. Tuomisto, Effect of interstitial carbon on the evolution of early-stage irradiation damage in equi-atomic FeMnNiCoCr high-entropy alloys, J. Appl. Phys. 127 (2) (2020), 025103.
[38] K. Arakawa, K. Ono, M. Isshiki, K. Mimura, M. Uchikoshi, H. Mori, Observation of the one-dimensional diffusion of nanometer-sized dislocation loops, Science 318 (5852) (2007) 956–959.
[39] S. Takaki, J. Fuss, H. Kuglers, U. Dedek, H.J.R.e. Schultz, The resistivity recovery of high purity and carbon doped iron following low temperature electron irradiation 79 (1–4) (1983) 87–122.
[40] A.L. Nikolaev, T.E. Kurennykh, On the interaction between radiation-induced defects and foreign interstitial atoms in α-iron, J. Nucl. Mater. 414 (3) (2011) 374–381.
[41] D. Terentyev, N. Anento, A. Serra, V. Jansson, H. Khater, G. Bonny, Interaction of carbon with vacancy and self-interstitial atom clusters in alpha-iron studied using metallic-covalent interatomic potential, J. Nucl. Mater. 408 (3) (2011) 272–284.
[42] B.N. Singh, A.J.E. Foreman, H. Trinkaus, Radiation hardening revisited: role of intracascade clustering, J. Nucl. Mater 249 (2–3) (1997) 103–115.
[43] S.J. Zinkle, G.S. Was, Materials challenges in nuclear energy, Acta Mater. 61 (3) (2013) 735–758.
[44] C. Barouh, T. Schuler, C.-C. Fu, M. Nastar, Interaction between vacancies and interstitial solutes (C, N, and O) in α– Fe: from electronic structure to thermodynamics, Phys. Rev. B 90 (5) (2014), 054112.
[45] G.M. Pharr, E.G. Herbert, Y.F. Gao, The indentation size effect: a critical examination of experimental observations and mechanistic interpretations, Annu. Rev. Mater. Res. 40 (2010) 271–292.
[46] R. Kasada, Y. Takayama, K. Yabuuchi, A. Kimura, A new approach to evaluate irradiation hardening of ion-irradiated ferritic alloys by nano-indentation techniques, Fusion Eng. Des. 86 (9–11) (2011) 2658–2661.
[47] W.D. Nix, H.J. Gao, Indentation size effects in crystalline materials: a law for strain gradient plasticity, J. Mech. Phys. Solid. 46 (3) (1998) 411–425.
[48] Y. Takayama, R. Kasada, Y. Sakamoto, K. Yabuuchi, A. Kimura, M. Ando, D. Hamaguchi, H. Tanigawa, Nanoindentation hardness and its extrapolation to bulk-equivalent hardness of F82H steels after single- and dual-ion beam irradiation, J. Nucl. Mater. 442 (1–3) (2013) S23–S27.
[49] H.Q. Zhang, C.H. Zhang, Y.T. Yang, Y.C. Meng, J. Jang, A. Kimura, Irradiation hardening of ODS ferritic steels under helium implantation and heavy-ion irradiation, J. Nucl. Mater. 455 (1–3) (2014) 349–353.
[50] X.B. Liu, R.S. Wang, A. Ren, J. Jiang, C.L. Xu, P. Huang, W.J. Qian, Y.C. Wu, C.H. Zhang, Evaluation of radiation hardening in ion-irradiated Fe based alloys by nanoindentation, J. Nucl. Mater. 444 (1–3) (2014) 1–6.
[51] X.D. Hou, A.J. Bushby, N.M. Jennett, Study of the interaction between the indentation size effect and Hall-Petch effect with spherical indenters on annealed polycrystalline copper, J. Phys. D Appl. Phys. 41 (7) (2008).
[52] N.D. Stepanov, N.Y. Yurchenko, M.A. Tikhonovsky, G.A. Salishchev, Effect of carbon content and annealing on structure and hardness of the CoCrFeNiMn-based high entropy alloys, J. Alloys Compd. 687 (2016) 59–71.
[53] C.Y. Chen, H.W. Yen, F.H. Kao, W.C. Li, C.Y. Huang, J.R. Yang, S.H. Wang, Precipitation hardening of high-strength low-alloy steels by nanometer-sized carbides, Mat Sci Eng a-Struct 499 (1–2) (2009) 162–166.
[54] C.L. Xu, L. Zhang, W.J. Qian, J.N. Mei, X.B. Liu, The studies of irradiation hardening of stainless steel reactor internals under proton and xenon irradiation, Nucl. Eng. Technol. 48 (3) (2016) 758–764.
[55] J. Benjamin, M.J.M.T.A. Bomford, Dispersion strengthened aluminum made by mechanical alloying 8 (8) (1977) 1301–1305.
[56] H.R. Higgy, F.H. Hammad, Effect of fast-neutron irradiation on mechanical properties of stainless steels: AISI types 304, 316 and 347, J. Nucl. Mater. 55 (2) (1975) 177–186.
[57] J.T. Busby, M.C. Hash, G.S. Was, The relationship between hardness and yield stress in irradiated austenitic and ferritic steels, J. Nucl. Mater. 336 (2–3) (2005) 267–278.
[58] X.D. Chen, Y.S. Li, Y.T. Zhu, B. Yang, Enhanced irradiation and corrosion resistance of 316LN stainless steel with high densities of dislocations and twins, J. Nucl. Mater. 517 (2019) 234–240.
[59] W.M. Mook, R. Raghavan, J.K. Baldwin, D. Frey, J. Michler, N.A. Mara, A. Misra, Indentation fracture response of Al-TiN nanolaminates, Mater Res Lett 1 (2) (2013) 102–108.
[60] C. Pokor, Y. Brechet, P. Dubuisson, J.P. Massoud, X. Averty, Irradiation damage in 304 and 316 stainless steels: experimental investigation and modeling. Part II: irradiation induced hardening, J. Nucl. Mater. 326 (1) (2004) 30–37.
[61] C.D. Hardie, C.A. Williams, S. Xu, S.G. Roberts, Effects of irradiation temperature and dose rate on the mechanical properties of self-ion implanted Fe and Fe-Cr alloys, J. Nucl. Mater. 439 (1–3) (2013) 33–40.
[62] O.J. Weiss, E. Gaganidze, J. Aktaa, Quantitative characterization of microstructural defects in up to 32 dpa neutron irradiated EUROFER97, J. Nucl. Mater. 426 (1–3) (2012) 52–58.